RELATIVE PERMEABILITIES FOR TWO- AND THREE PHASE FLOW PROCESSES RELEVANT TO THE DEPRESSURIZATION OF THE STATFJORD FIELD

Egil Boye Petersen Jr[(1)], Arild Lohne[(2)], Kåre O. Vatne [(2)],
Johan Olav Helland[(2)], George Virnovsky[(2)] and Pål-Eric Øren[(3)]
[(1)] Statoilhydro ASA and [(2)] IRIS, [(3)] Numerical Rocks AS

ABSTRACT

This paper presents an extensive experimental study of relative permeability functions of two- and three-phase displacement processes relevant to the depressurisation of the Statfjord Field. The measurements were performed on reservoir core material and under full reservoir conditions to ensure representative wettability and spreading conditions. A total of five two-phase and six three-phase steady state relative permeability data sets are reported. Three-phase relative permeabilities were measured for both drainage dominated (increasing S_g) and imbibition dominated (decreasing S_g) three-phase flow.

All of the three-phase flow experiments were successfully history matched using a steady state core flood simulator. Independently measured capillary pressure functions were used to properly account for capillary pressure effects in the experiments. The results show that commonly used empirical models that predict three-phase relative permeabilities from two-phase data (e.g. Stone 1 and saturation weighted interpolation) are not able to accurately describe the three-phase experiments. This confirms that phase saturation and saturation history are major factors in determining three-phase relative permeabilities.

INTRODUCTION

Depressurisation of the Statfjord Field is considered to be an option to increase the oil and gas reserves from the field and to extend field life. The depletion of reservoir pressure below bubble point allows solution gas to liberate from the remaining oil in the reservoirs. The liberated gas will then segregate towards structural highs and create secondary gas caps, which can further be produced. To accurately model these processes, knowledge of three-phase relative permeabilities and the critical gas saturation for mobilization of gas are of paramount importance [1].

On the core-scale, three-phase relative permeabilities can be obtained from laboratory measurements. However, these experiments are often time consuming and technically difficult to perform, especially under reservoir conditions. In addition, it is impractical to measure three-phase relative permeabilities for all possible three-phase displacement paths that can occur in the reservoir. As a result, three-phase relative permeabilities are almost always estimated from two-phase data on the basis of empirical models. The empirical nature of these models constitutes a major deficiency in the theory of three-phase flow in porous media and limits our ability to accurately predict three-phase flow in the reservoir.

Many of the most frequently used empirical models were developed for water wet media. Furthermore, available experimental data sets used for testing and validation of these models typically stem from measurements on water wet outcrop rocks [2-6]. However, reservoir rocks are rarely water wet and empirical models often fail to accurately predict three-phase relative permeability for reservoir rocks.

Empirical models fail because they do not fully account for the physics of three-phase flow. Depending on wettability and spreading conditions, the pore occupancy and phase continuity in three-phase flow can be significantly different than that represented by the corresponding two-phase experiments. True prediction of three-phase relative permeability from two-phase data can thus not be assured, regardless of how sophisticated the model is.

In this paper we present a series of two-phase and three-phase steady state relative permeability measurements performed under reservoir conditions and at representative mixed wettability conditions. The measured data are interpreted using a simulator that utilizes independently determined capillary pressure functions to account for capillary end effects. The history matched three-phase relative permeabilities are compared with those predicted from two-phase data on the basis of empirical models. This work provides important new data for developing and testing models of three-phase relative permeability for reservoir rocks.

EXPERIMENTAL

Apparatus

The schematic of the flow apparatus is shown in Figure 1. It consists of a pumping system, a three-phase separator, a core holder and an X-ray system for in-situ saturation measurements. Each of these components is described below. For further details on the experimental set-up, see Ebeltoft *et al*. [2].

The *pumping system* consists of eight computer-controlled cylinders that have the capability of recycling three phases simultaneously through a core sample. The cylinders are paired, and three cylinder pairs are used for recycling water, oil and gas through the core sample. The seventh cylinder is working in a constant pressure mode, and acts as a back pressure regulator within 7 kPa accuracy. This cylinder is connected to the water return line, but is in contact with the other phases indirectly through the separator.

The *core holder* is placed inside the heated cabinet with possibilities of tilting either in horizontal position or in vertical position with the inlet at the top. The core sample is placed between two distribution plugs. Both plugs have ports for monitoring the differential pressure between the end faces of the core sample. Several rubber washers are placed behind each distribution plug to transmit an axial stress proportional to the confinement pressure.

Water, oil and gas productions were measured with *a three-phase acoustic separator*. Two pressure transmitters with range 0-0.3 bar and 0-7 bar, respectively, were used to measure the differential pressure across the core. The pressure ports are placed directly at the inlet and the outlet ends of the core. The X-ray system was not used during experimentation.

Procedures
In this study, a total of six steady-state measurement series, with two or three phases flowing, have been performed in a composite core at relevant reservoir conditions, 200 bar and 91°C. To obtain a representative reservoir fluid, separator oil and gas were sampled at the platform test separator. The brine used is synthetic formation water. Core and fluid properties measured at test conditions are given in Tables 1 and 2. The steady-state series were designed to cover two main processes relevant for the field during depressurisation below bubble point pressure and in alternating gas-water injection. Five of the series contain a hysteresis cycle with increasing S_g in the first part and decreasing S_g in the second part. The first reservoir process covered represents a secondary displacement with gas conducted after a primary water flood. This process is denoted **DDI** indicating **D**ecreasing S_w, **D**ecreasing S_o and **I**ncreasing S_g. The second part of the experiment covers the reverse process **IID** (**I**ncreasing S_w, **I**ncreasing S_o and **D**ecreasing S_g).

Initial S_{wi} was established by porous plate and 5 bar P_{cow}, and later before each new **DDI** series, approximately re-established by viscous flooding using STO to remove free gas. Initial conditions for each **DDI** series is then established by injecting water/oil at a fixed ratio. A list of all the measurements series is given in Table 3.

Results
Figure 2 shows the saturation trajectories from all the series plotted in a ternary diagram. The points represent the average saturations in the core after steady-state conditions are reached (SS-points). In the series with two phases injected the third phase is termed **C**onstant. This "constant" phase saturation may in reality be reduced, but obviously it cannot increase. From the figure we see that in the **CDI**+**CID** series (gas/oil flood at S_{wi}) the water saturation remained constant, while in **DCI**+**ICD** (gas/water flood at S_{orw}) additional oil is produced at both increasing and decreasing S_g. The computations of the relative permeability functions are described in the next section.

COREFLOW SIMULATION
Steady state history matching
All the three-phase relative permeability experiments have been simulated with the steady-state core-flood simulator Coreflow [7, 8]. This is done to correct the computed relative permeabilities for the presence of capillary forces. The result is compared against the relative permeability computed from Darcy's law, neglecting capillary effects.

The Coreflow simulator requires explicit input of the capillary pressure together with experimental data obtained at steady state (saturations and pressure drops). Relative permeability functions are then computed by minimizing the difference between computed and measured saturations and pressure drops**.** The relative permeability is represented by single-argument functions ($k_{rj}(S_j)$, $j=w,o,g$) of either Corey type or on tabular form using linear interpolation or quadratic splines. In this study we typically use quadratic splines to represent $\mathrm{d}(\log(k_{rj}))/\mathrm{d}S_j$ at four fixed saturation points and a fixed k_{rj}-value at the lowest saturation. With three phases, the total number of matching parameters is then twelve.

In three-phase flow, the relative permeability of a phase will in general depend on two saturations. However, single-argument functions should be sufficient to describe the relative permeabilities along a single saturation trajectory obtained in one three-phase series. A necessary requirement, which is satisfied (see Figure 2), is that the saturation trajectory is monotonous with respect to the saturation development for all phases. Separate simulations are then run for each three-phase series.

Capillary pressure
An example of capillary pressure functions used in the simulations of series **DDI-1** and **IID-1** is given in Figure 3 in dimensionless form (*J*-scaled). The capillary pressure in bar is given by $P_{ci} = 0.318 \cdot \gamma_i \sqrt{\phi/K} J_i$, $i=(ow, go)$, with units mD for the permeability (see Table 1.) and mN/m for the interfacial tension (Table 2.). The boundary curves for water (J_{owI}: imbibition and J_{owD}: secondary drainage) and the primary gas drainage curve (J_{goD}) are obtained from measured capillary pressure on neighbouring cores. The *J*-scaling is applied to account for differences in porosity, permeability and interfacial tension. The measured oil/water imbibition and secondary drainage curves are obtained in centrifuge after spontaneous imbibition with crude oil and synthetic brine at 60ºC. The gas/oil primary drainage curve is measured with air/white oil at ambient conditions in centrifuge.

A typical experimental series starts at some initial water saturation (first obtained by porous plate, later by viscous flooding). Then there is a two-phase flood along the oil/water base line ($f_w=f_o=0.5$ in **DDI-1**) to establish the starting point for the increasing S_g part. Next, the injection ratio between water and oil is kept constant ($f_w/f_o=1$ in **DDI-1**) while f_g is increased in steps. The appropriate oil/water capillary pressure for this **DDI** process will start (approximately) at the boundary imbibition curve and follow a scanning curve crossing over towards the boundary drainage curve as indicated by J_{ow}-DDI-1 in Figure 3. The oil/gas drainage capillary pressure which is used in all the series with increasing S_g is described by the J_{goD}-curve. Then the process is reversed and the gas fraction is stepwise reduced down to zero. The capillary pressure curves will then be imbibition scanning curves (J_{ow}-IID-1 and J_{go}-IID-1) starting from some reversal point at the previous curves.

The capillary pressures for the different series are computed from the boundary curves and the previous saturation history approximated by the average experimental saturations at process reversals. A model proposed by Killough [9] which is readily applied to capillary pressure data on free (tabular) form is slightly modified to allow for problem-free nested scanning curves. The capillary pressure can be expressed in the general form

$$P_c = P_{c,I} + F\left[P_{c,D} - P_{c,I}\right], \text{ with } F = F_1 + \left(F_2 - F_1\right) \frac{\left(\left|S_w - S_w^{H1}\right| + \varepsilon\right)^{-1} - \dfrac{1}{\varepsilon}}{\left(\left|S_w^{H1} - S_w^{H2}\right| + \varepsilon\right) - \dfrac{1}{\varepsilon}}. \qquad (1)$$

$P_{c,D}$ and $P_{c,I}$, are obtained from the drainage and imbibition boundary curves at the same saturation (S_w). F is obviously equal to one along the drainage boundary curve, and zero along the imbibition boundary curve. Two variables must be remembered from all n_{rev}

previous reversals, S_w^{Hi} and F_i (i=1,2, ...,n_{rev}). The numbering is organized so that the last reversal is 1 and the previous is 2, and so on. A value of 0.05 is used for the "*curvature*" parameter ε (0.05-0.1 recommended by Killough).

History matching results
The results of the history matching are presented in details for two series, **CDI** (gas flood at S_{wi}) and **DDI-1** (three-phase flood with increasing S_g). Relative permeabilities, corrected for capillary forces, for all the experimental data sets are presented in the form of isoperms plotted in ternary diagrams in Figure 10 to Figure 15. Each phase (oil, water and gas) is represented by two plots displaying the **DDI** process and the **IID** process respectively. The two- and three-phase relative permeabilities are also plotted as a function of their own phase saturation in Figure 26 to Figure 28. The results clearly suggest that the oil, water and gas relative permeabilities each depends on more than its own phase saturation.

Examples of how the simulated relative permeability compares to the values computed from Darcy's law without correction for capillary forces are given in Figure 4 and Figure 5 for series **CDI** and **DDI-1**, respectively. Figure 6 and Figure 7 show afairly accurate reproduction of the experimental saturations and pressure drops over the core. We observe that capillary end effects are only significant for the two last points in Figure 4 and the last point in Figure 5 when only gas is injected. This is partly a result of high pressure drops dominating over capillary forces in most of the experiment, but also because the relative permeability of a phase can only influence its saturation if that phase is flowing.

Figure 8 shows the simulated gas saturation profiles through the core in **CDI**. We observe constant saturation through the core when both oil and gas are flowing (SS-point 2-7) except in a small part towards the outlet end. The profiles are dominated by the relative permeability characteristics, and the capillary end effects are small. However, in SS-point 8 and 9, when only gas is injected, then the saturation profile of the non-flowing oil phase is fully governed by the balance between capillary forces (P_{cgo}) and viscous forces caused by the gas flow. The capillary pressure used, represented by J_{goD} in Figure 3, gives a satisfactory reproduction of the two last experimental oil saturation points in Figure 6. In particular we note that the rate dependency of remaining oil at the core scale is nicely captured when the gas injection rate is increased from 5 to 15 ml/min (SS-point 9). This rate dependency caused by core end effects makes it very hard to quantify the true S_{org} valid at the field scale. We only know that it must be lower than the average saturation at the last SS-point (S_o=0.148). To illustrate the uncertainty, we can mention that the S_{org} from capillary pressure used in the simulations was 0.04 and the simulated inlet S_o for SS-point 9 was as low as 0.073.

The **DDI-1** series has two non-flowing phases, oil and water, in the last SS-point 8 (see Figure 7). Their average saturations (S_w=0.310, S_o=0.218) are well beyond what is expected to be their residual saturations, i.e., the amount of remaining oil and water should be a result of the balance between viscous and capillary forces similar to that described for the **CDI** series above. However, to fairly match the experimental saturations it was necessary to use an artificial high value for residual oil (S_{or}=0.19). Simulated saturation

and pressure profiles for SS-point 8 are plotted in Figure 9. Both S_g and S_w varies through the core. The S_o profile, expected to be a result of capillary versus viscous forces, is in stead flat and equal to the input S_{or} except near the outlet. We also observe that the simulated oil pressure is nowhere close to its hydrostatic gradient, which should be the case for a non-flowing yet mobile phase.

High artificial S_{or} had to be used in simulation of the other three-phase series as well, 0.25 in **DDI-2** and 0.10 in **DDI-3**. These **DDI** series were ended with a rate increase from 5 to 15 ml/min at f_g=1. The measured and simulated average saturation responds are shown in Table 4. We observe that the experimental rate dependency in remaining oil is not captured in the simulations. The computed S_o is practically the same for the two rates and equal to the input S_{or}. The artificial S_{or} represents a compromise trying to minimize the total error in computed S_w and S_o for all the SS-points. The average S_o at the higher rate (SS-point 10) is 0.257 in **DDI-2** and 0.078 in **DDI-3**.

These observations are strongly indicating that the two-phase capillary pressure representation used for P_{cow} and P_{cgo} are insufficient to fully describe capillary pressure in three-phase flow. It also seems reasonable to expect the three-phase dependency to be increasingly important at low oil saturations where gas/water interfaces are more likely.

If a non-flowing phase is still continuous inside the formation, it will also be mobile. Its saturation will be governed by spatial variations in capillarity (e.g., core end effects) and balance between viscous, gravitational and capillary forces. If we assume the oil to be mobile, but capillary trapped due to core end effects, in series **DCI** (gas flood at S_{orw}) then we can compute the P_{cgo} at the inlet end to be $P_{cgo\_in} = p_{in} - p_{out} + (\rho_o - \rho_g)gL$. If oil is produced from one step to the next increased f_g, then P_{cgo} at the inlet will be as computed, otherwise actual inlet P_{cgo} must be larger than P_{cgo_in}. This inlet P_{cgo} estimated from pressure data is plotted in Figure 16 together with the two-phase gas-oil capillary pressure computed from average saturation ($P_{cgo}(S_g)$ at S_{wi}). Also included in the figure is the average S_o obtained at each steady-state step. These results indicate that P_{cgo} at high S_w is an order of magnitude higher than measured at S_{wi}. The observed oil production during the **DCI** and **ICD** experiments supports the assumption of a continuous and mobile oil phase. We observe that oil production more or less stops after a maximum in the P_{cgo_in} is passed in **DCI**, but that additional oil is produced when this maximum is exceeded in **ICD**.

Similar estimation of inlet P_{cow} for **DCI** and **ICD** plotted in Figure 17 indicates that the actual oil-water capillary forces can be much larger in three-phase flow compared to $P_{cow}(S_w)$ at zero S_g. The results show a significant vertical shift in P_{cow} towards increased negative values and a shift in the zero P_{cow}-point towards lower S_w when gas is present.

ECLIPSE SIMULATION
Numerical model
The black oil simulator Eclipse 100 was used to validate the experimentally determined three-phase relative permeabilities by simulating the full history of the steady-state experiments. These results are then compared with those obtained when the corresponding three-phase relative permeabilities are estimated from two-phase data by two frequently

used empirical correlations: Stone 1 [10] and the saturation weighted interpolation model proposed by Baker [11].

The composite core was represented by 204 grid blocks oriented vertically with the inlet at the top and the outlet at the bottom. Two additional blocks having zero capillary pressure were used to capture the core end effects at the inlet and outlet. The injection and production wells were located in these blocks. The capillary pressure is selected according to the previous saturation history, e.g., for experiment **DDI-1** the curves in Figure 3 are used. All the relative permeabilities used are the ones corrected for capillary effects.

Interpolation methods (Baker and Stone)
The relative permeability to water and gas are obtained from the two-phase oil/water (**IDC**) and gas/oil (**CDI** at S_{wi}) series, respectively. The oil relative permeability is interpolated from the same two-phase data sets using Stone 1 & 2 or saturation weighted interpolation (Baker). The predicted k_{ro} with these models are shown in Figure 23, Figure 24 and Figure 25. The simulation of experiment **DDI-1** is shown in Figure 18 (Baker), Figure 19 (Stone 1) and Figure 20 (Stone 2). The figures show experimental and simulated development of average saturations and pressure drop over the core (Δp).

The saturation weighted method gives a reasonable reproduction of the experimental S_o, while the simulated S_w is over predicted and the S_g under predicted. The Δp is under estimated with roughly 30-40% in most of the experiment.

The Stone 1 method produces even poorer results with all three saturations far away from the measured ones during most of the run. The simulated Δp is less than half the measured value. The Stone 2 results are of similar quality, but with the distinct difference that oil production stops when S_o reaches 33% in consistency with the isoperms in Figure 25.

Three-phase data
The relative permeability to oil is entered in form of a two-dimensional table versus S_w and S_g using the Eclipse keyword SOF32D. The appropriate data set for simulation of the **DDI** process is given in Figure 10. Some minor modifications were necessary in form of removing non-monotonic behaviour that is not accepted in Eclipse. The oil isoperms interpolated from the final table is shown in Figure 22.

The measured relative permeability to both water and gas were also full three-phase functions. An alternative to using the full three-phase functions as displayed in Figure 12 (water) and Figure 14 (gas) is to use single-argument functions obtained along the experimental saturation path. Then the three-phase dependency is included in the simulations by selecting the appropriate curves for each series. The curves used for water and gas in simulation of the **DDI-1** experiment are the ones given in Figure 5.

The tabulated values of three phases relative permeability gives an excellent match to both experimental saturations and the differential pressure drop over the core, except for some differences in saturations at the final injection rate where only gas is flowing (Figure 21). These results compare well with the match obtained by steady-state simulation in Figure 7.

CONCLUSION

- A new three phase relative permeability data set corresponding to the depressurization process in the Statfjord field has been presented.
- The measured three phase data has been interpreted using a simulator where the independently obtained capillary pressure functions are utilized to account for the capillary end effects.
- The assumption that two phase relative permeability data can be used to predicted three phase relative permeability following the same saturation history seems questionable and should always be validated by laboratory testing.
- Using experimentally determined three phase relative permeability data, adjusted for capillary end effects, as tabulated input in reservoir simulators seems to give improved results in modelling of three phase flow.
- The failure of two-phase capillary functions to represent three-phase capillary pressure is demonstrated. Three-phase capillary pressures may be significantly larger than their two-phase counterparts, and make correct determination of residual oil saturation difficult.

ACKNOWLEDGEMENTS

REFERENCES

1. E.B. Petersen Jr, G.S. Agaev, B. Palatnik, J.K. Ringen, P.E. Øren, and K.O. Vatne, "Determination of critical gas saturation and relative permeabilities relevant to the depressurisation of the Statfjord field," International Symposium of the Society of Core Analysts, Abu Dhabi, UAE, 2004.
2. E. Ebeltoft, J.E. Iversen, K.O. Vatne, M.A. Andersen, and J.E. Nordtvedt, "A Novel Experimental Apparatus for Determination of Three-Phase Relative Permeabilities at Reservoir Conditions," the International Symposium of the Society of Core Analysts, Montpellier, France, 1996.
3. M.J. Oak, "Three-Phase Relative Permeability of Water-Wet Berea," SPE 20183 presented at SPE/DOE Symposium on Enhanced Oil Recovery, Tulsa, USA, 1990.
4. M.J. Oak, "Three-Phase Relative Permeability of Intermediate-Wet Berea Sandstone," SPE 22599 presented at SPE Annual Technical Conference and Exhibition, Dallas, Texas, USA, 1991.
5. M.J. Oak, L.E. Baker, and D.C. Thomas, "Three-Phase Relative Permeability of Berea Sandstone," *J. Pet. Tech.*, vol. 42, pp. 1054-106, 1990.
6. M.J. Oak and R. Ehrlich, "A New X-Ray Absorption Method for Measurement of Three-Phase Relative Permeability," *SPE Reservoir Engineering*, vol. 3, pp. 199-206, 1988.
7. G.A. Virnovsky, J. Mykkeltveit, and J.E. Nordtvedt, "Application of a steady-state three-phase simulator to interpret flow experiments," International Symposium of the Society of Core Analysts, Montpellier, France, 1996.
8. G.A. Virnovsky, K.O. Vatne, S.M. Skjæveland, and A. Lohne, "Implementation of multirate technique to measure relative permeabilities accounting for capillary effects," SPE 49321 presented at the SPE Annual Technical Conference and Exhibition, New Orleans, Louisiana, 1998.
9. J.E. Killough, "Reservoir Simulation With History-Dependent Saturation Functions," in *Trans*. AIME, vol. 261, 1976, pp. 37-48, (*SPEJ* , Feb., **16**).
10. H.L. Stone, "Probability Model for Estimating Three-Phase Realtive Permeability," *J. Pet. Tech.*, pp. 214-218, 1970.

11.   L.E. Baker, "Three-Phase Relative Permeability Correlations," SPE 17369 presented at the SPE/DOE Enhanced Oil Recovery Symposium, Tulsa, Oklahoma, USA., 1988.

Table 1: Composite core data and experimental conditions.

Core assembly		Conditions	
Length (cm):	27.29	Temperature (ºC):	91
Diameter (cm):	3.75	Net confining pressure (bar)	150
Pore volume (cm^3):	95.9	Pore pressure (bar)	200
Porosity (frac.):	0.318		
Absolute permeability (mD)	873		
S_{wi} (porous plate 5 bar):	0.189		
Oil permeability at S_{wi} (mD)	456		

Table 2: Fluid data (measured at 91 ºC and 200 bar).

	Water	Oil	Gas
Density (g/cc)	1.0013	0.6911	0.1642
Viscosity (cP)	0.336	0.423	0.0218
	oil/water	gas/oil	gas/water
Interfacial tension[*] (mN/m)	23.1	3.8	22.5

*) Pendent drop method at test conditions (91°C and 200 bar).

Table 3: Experimental series in the order performed.

Series[*]	Water: Oil ratio	Description
CDI + **CID**	-	gas/oil flood at S_{wi}
IDC	-	water/oil flood
DCI + **ICD**	-	gas/water flood at S_{orw}
DDI-1 + **IID-1**	1:1	three-phase flood at intermediate S_w
DDI-2 + **IID-2**	6:94	three-phase flood at low S_w
DDI-3 + **IID-1**	94:6	three-phase flood at high S_w

*) Letters indicate change in fractional flow to water, oil and gas during the experiment: **D**ecreasing, **I**ncreasing or **C**onstant (not injected).

Table 4: Measured (exp) and simulated (calc) average saturations for the last two SS-points in DDI-2 and DDI-3 where rate is increased at 100% gas injection.

		Qt	Swa	Soa	Swa	Soa
		ml/min	exp	exp	calc	calc
DDI-2	SS-point 9	5	0.274	0.297	0.290	0.255
	SS-point 10	15	0.257	0.257	0.290	0.251
DDI-3	SS-point 9	5	0.440	0.120	0.445	0.102
	SS-point 10	15	0.408	0.078	0.386	0.102
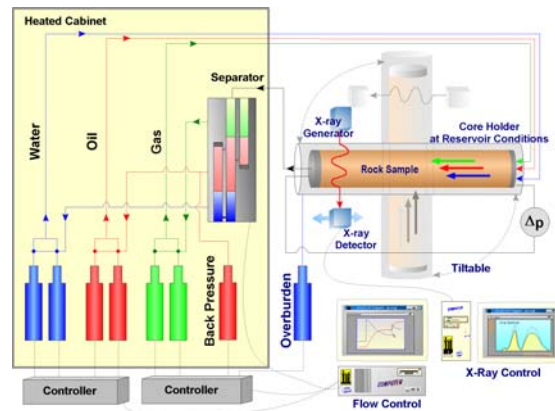
Figure 1: Three-phase flow apparatus**.**
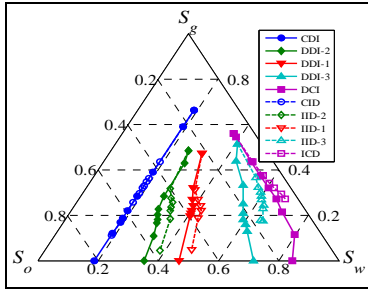
Figure 2: Experimental saturation paths.
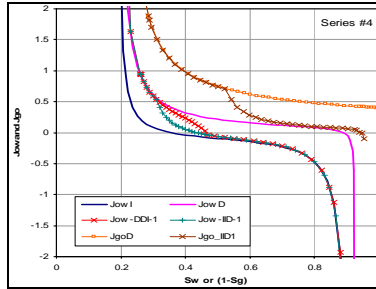
Figure 3: Capillary pressure used in DDI-1/IID-1.
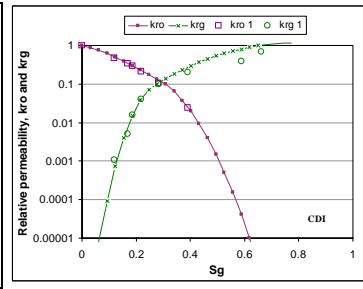
Figure 4: CDI: Relative permeabilities computed with and without (1) correction for capillary forces.
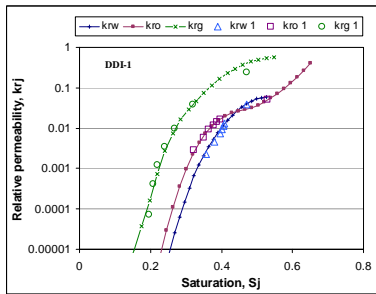
Figure 5: DDI-1: Relative permeabilities computed with and without (1) correction for capillary forces.
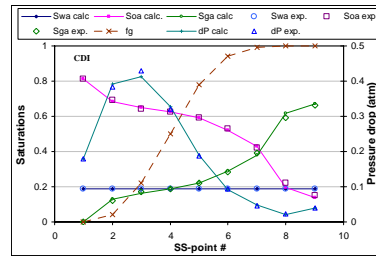
Figure 6: CDI: Experimental and simulated saturations and pressure drops.
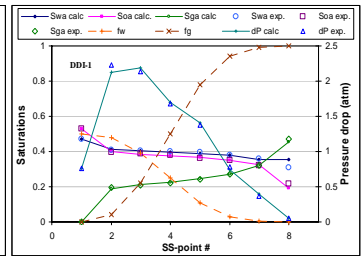
Figure 7: DDI-1: Experimental and simulated saturations and pressure drops.
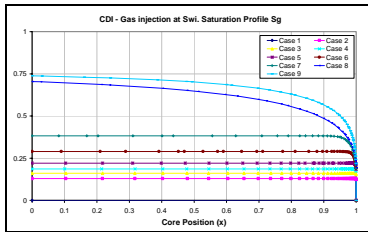
Figure 8: Simulated gas saturation profiles in the **CDI** - series, flow direction: left to right. Total flow rate is 5 ml/min (point 1-8) and 15 ml/min (point 9).
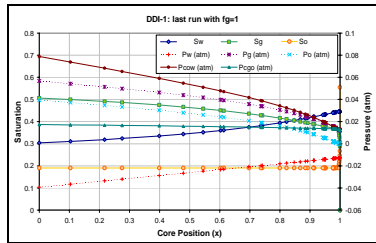
Figure 9: Simulated saturation and pressure profiles in the last **DDI-1** SS-point with 100% gas injection (f_g=1). Total flow rate is 8 ml/min.
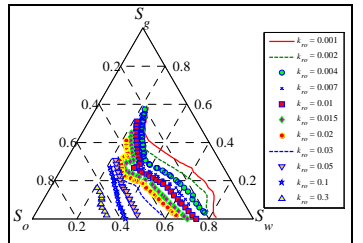
Figure 10: K_{ro} isoperms estimated from DDI - series.
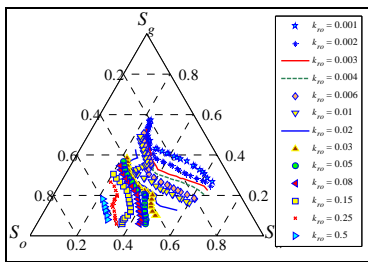
Figure 11: K_{ro} isoperms estimated from IID - series.
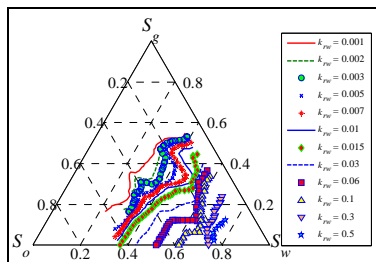
Figure 12: K_{rw} isoperms estimated from DDI - series.
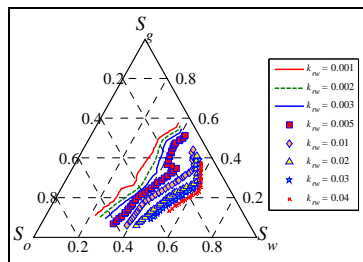
Figure 13: K_{rw} isoperms estimated from IID - series.
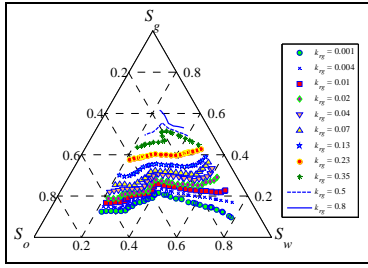
Figure 14: K_{rg} isoperms estimated from DDI - series.
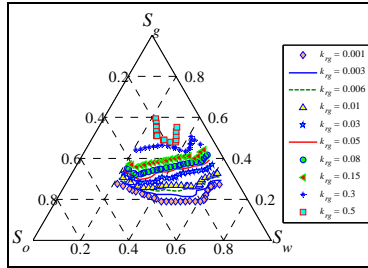
Figure 15: K_{rg} isoperms estimated from IID - series.
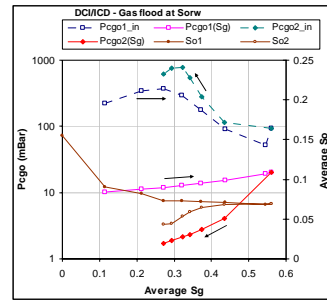
Figure 16: P_{cgo} estimated at core inlet from Δp and from average S_g. 1: increasing and 2: decreasing S_g.
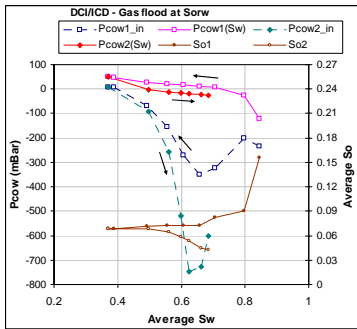
Figure 17: P_{cow} estimated at core inlet from Δp and from average S_w. 1: decreasing and 2: increasing S_w.
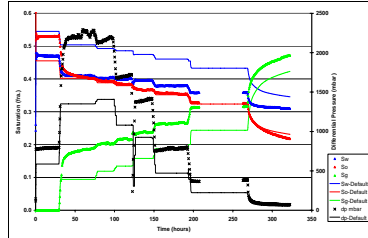
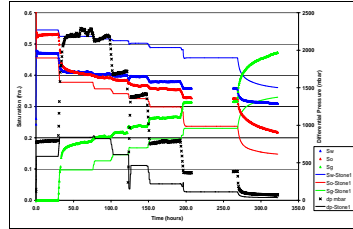**Figure 18:** DDI-1:Experimental and simulated (Baker) average saturations and differential pressure.

Figure 19: DDI-1:Experimental and simulated (Stone1) average saturations and differential pressure.
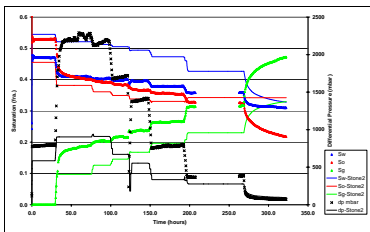
Figure 20: DDI-1:Experimental and simulated (Stone2) average saturations and differential pressure.
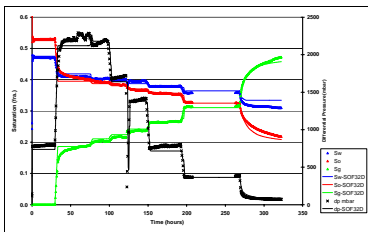
Figure 21: DDI-1:Experimental and simulated (SOF32D) average saturations and differential pressure.
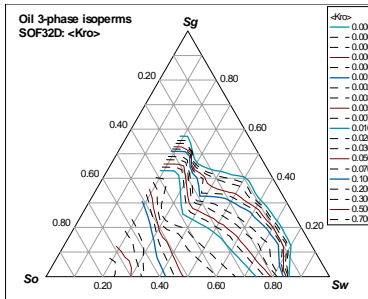
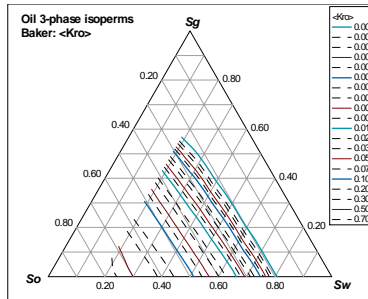**Figure 22**: Three-phase k_{ro} with SOF32D table.

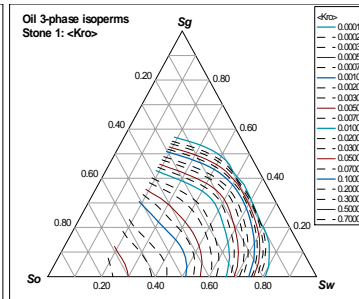**Figure 23**: Three-phase k_{ro} with default option in Eclipse (Baker's model).

Figure 24: Three-phase k_{ro} with Stone 1 model.
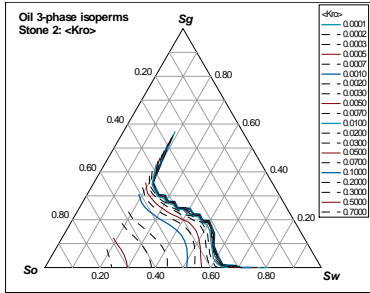
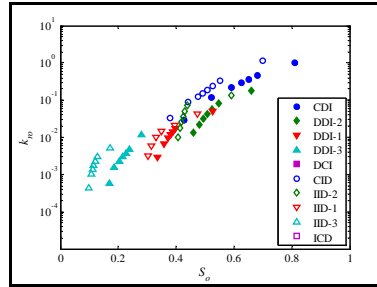**Figure 25:** Three-phase k_{ro} with Stone 2 model.

Figure 26: Two and Three-phase k_{ro}. Corrected for capillary end effects.
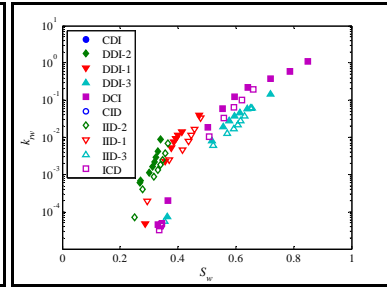

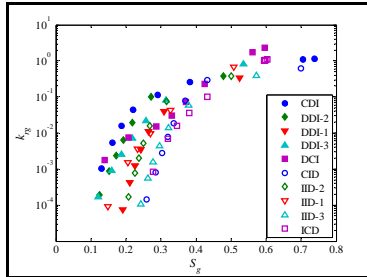**Figure 27:** Two and Three-phase k_{rw}. Corrected for capillary end effects.

Figure 28: Two and Three-phase k_{rg}. Corrected for capillary end effects.